GG2: CT Reconstruction and Visualisation
Final Report

Sanchit Gandhi
Group 1: S. Gandhi, J. Olieslagers, M.Y.Z. Wong
CRSiD: sg836
Queens' College

June 4, 2020

Summary

This report documents the second half of the X-Ray Computed Tomography (CT) Reconstruction and Visualisation project, in which the previously developed CT simulator was used to reconstruct 'real-life' raw data of an action figure obtained from a micro-CT scanner. Effective visualisations of the reconstructed 3D CT data were made through the use of freely available software. Having segmented the figurine into its constituent body parts, a treatment plan involving the transplant and fitting of a human heart was established. By generating the surface for each part, including the heart to be fitted, the process of 3D printing the subject was simulated. Print settings were allocated on a body part basis, by considering model intricacy and relevance to the transplant, giving a suitable balance of print time and resolution. With access to a 3D printer, the final files could be used to reproduce the body parts of the action figure in its entirety.

1 Introduction

CT is a powerful imaging modality, in which measurements of X-ray intensities through a subject are taken at many angles and offsets, such that anatomical information is projected onto a 2D plane. *Image reconstruction* is a mathematical procedure used to find the original attenuation distribution from an acquired data, from which 3D visualisations of slices through the attenuation field can be made. These visualisations are invaluable to a clinician, as they outline the internal structure of a patient, enabling the development of appropriate treatment plans.

Issues regarding raw CT data, such as sampling, noise and beam hardening, as well as complications that arise in the filtered back-projection (FBP) reconstruction process, namely resolution, interpolation, and filter form, were discussed at length in the Interim Report. In reconstructing the 'real-life' CT data, several further simplifications and approximations were made. The investigations that follow look at the impact of these limitations on the reconstructed data, and the subsequent implications on the accuracy of treatment plans.

In addition to reconstruction, the tasks of *visualising* and *modelling* the data were explored. This involved the appropriate selection of free to use applications by considering ease-of-use, features available and compatibility of file formats. The main parameters relevant to the 3D printing process were varied and the effects on print cost and print time quantified. The results of these investigations were used to devise a set of printer configurations that gave higher strength models for the parts relevant to the heart transplant procedure, and faster, weaker prints for the others.

2 Real CT Data

Raw CT data of an Action Man action figure was obtained through the use of an Xtreme micro-CT device, a high-resolution peripheral quantitative CT system [4]. Compared to the 1st-generation translate-translate CT device on which the CT simulator was based, the micro scanner is a 3rd-generation device, operating on a rotate-translate scheme with a 60 kVp energy distribution of X-rays. Being much smaller in dimension but of higher resolution, the CT data is similar to that of a full-scale scanner. A labelled schematic of the scanner and its *cone-beam* configuration is shown in Fig. 1, an excerpt from the project handout.

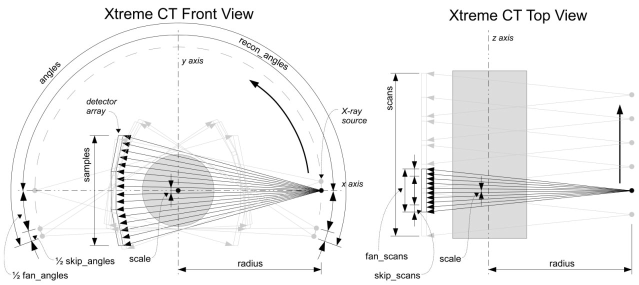

Figure 1: Diagrammatic representation of the SCANCO Medical Xtreme CT scanner, taken from the project handout.

The figurine was mounted in an acrylic cylinder for the data acquisition process to maintain a fixed position within the scanner. Since it did not fit within the device in its entirety, it was scanned in two halves, giving two sets of unaligned, raw data in '`.rsq`' file form, referred to as 'data set a' and 'data set b' respectively.

3 Reconstruction

The previously completed CT simulator was modified to reconstruct the raw CT data by completing the inner-loop within the `reconstruct_all` function from the `Xtreme` class. Each group member attempted this task individually, before meeting to discuss implementations and settling on a final code form. The following solution is the one devised by myself, which was agreed to be the code to be used going forwards for the rest of the project.

The right diagram in Fig. 1 shows the diverging nature of a cone-beam scanner in the z-direction. For reconstruction, the X-rays were presumed to be parallel in this direction, justifiable as the beam angle is relatively small. The errors introduced in making this simplification were investigated following completion of the reconstruction function.

No longer requiring the generation of a phantom image or the modelling of the scanning procedure, the first step in the process involved calibrating the acquired data. For every X-ray source z location, `get_rsq_slice` was called to return the fan-based sinogram f of residual intensities, in addition to a detection along an angle with the source completely off f_{min} and one with it fully on with the scanner left empty f_{max}. Noise from the measurements was removed by subtracting f_{min} from both f and f_{max}. The new values of f and f_{max} were used to air calibrate the sinogram, converting it to attenuation values, as outlined in eq. (4) of the interim report and previously performed by the `ct_calibrate` function.

The calibrated fan-based sinogram was transformed to a parallel sinogram using the `fan_to_parallel` function provided. The FBP procedure was unchanged from before, first filtering with a band-limited raised-cosine filter before back-projecting to yield a 2D cross-sectional image of the slice, with the returned array values corresponding to the measured attenuations for each pixel.

Rather than performing a scan through a water phantom, conversion to Hounsfield units was achieved by making use of the acrylic cylinder in which the action figure was scanned. The 25^{th} slice of data set a is a disk of acrylic, as shown in Fig. 2. This slice was reconstructed, and the output array windowed to give attenuation values characteristic of acrylic for X-ray energies below 60 keV. This range was chosen based on the fact that the source distribution is 60 kVp, as stated by the device manufacturer [4]. The average of these windowed values was found to be 0.241, which corresponds to an X-ray energy of 53.7 keV. The linear attenuation coefficient of water for this energy was found by means of linear interpolation, the value of which was used to perform the Hounsfield conversion. Finally, the reconstructions were saved as DICOM files, through use of the `create_dicom` function.

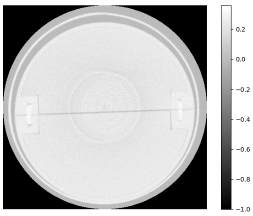

(a)

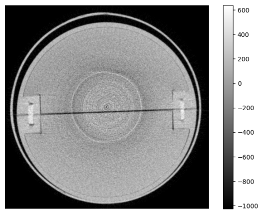

(b)

Figure 2: Reconstructions of slice 25 of data set a. (a) Linear attenuation values. (b) Hounsfield values.

With a complete reconstruction function, Wong and I investigated errors introduced in making the presumption that the X-ray beams were parallel in the z-direction. This was achieved by reconstructing individual slices for different positions along the fan beam for a given slice location and making visual assessments of the accuracy and artefacts present in the returned images. Since the centre of the cone-beam is directly opposite the X-ray source, it is a parallel beam. As a result, there are no errors in the reconstruction from making the parallel beam presumption, and so these slices are reconstructed perfectly. On the contrary, the extremities of the beam diverge by the greatest angle from the source. These are also the locations where the beams from neighbouring source positions overlap and differ by twice the beam angle, making them the ones with the largest errors.

The parameters of the fan beam were found using the `Xtreme` class on the raw CT data. With 41 z-axis scans in each z-fan group and 3 scans at each end of each z-fan which overlap with the neighbouring z-fan, the investigation focused on the 3 slices either side of multiples of 41. There were no obvious errors when the image reconstructions themselves were inspected. We, therefore, turned to look at the differences between adjacent slices, both for fan centres and edges, the results of which are shown in Fig. 3.

Progressing through slices gives cross-sectional images at different positions in small intervals. Looking at slices 429 to 434, those situated around the centre of the fan, there are only slight geometrical changes between images, with consistent regions of high and low attenuation. This is as expected, given the action figure is continuous and constructed of portions of material with the same attenuation coefficient. However, there are stark differences between slices 451 to 452, those at which one z-fan ends and the next begins. This can be seen in the bottom image from the bottom row of Fig. 3, where the Hounsfield values of the rightmost feature change dramatically, and rectangular regions of different attenuation are streaked across the central and leftmost

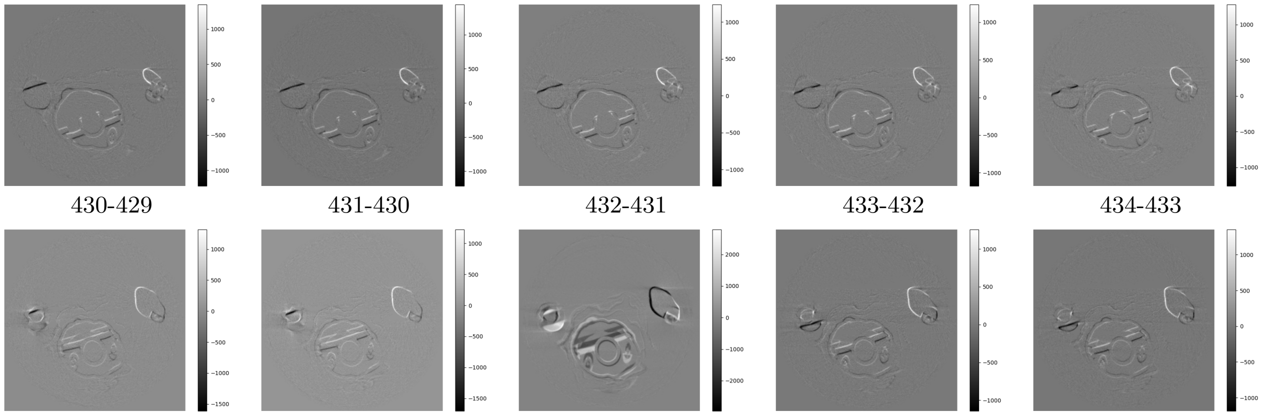

Figure 3: Difference in reconstructions for adjacent slices for data set a. Top row: fan centre. Bottom row: fan edge.

structures. Such artefacts were found at the end of every fan-beam, and can be corrected for by implementing *Parallel Feldkamp-Davis-Kress* (P-FDK) reconstruction, details of which are outlined in Turbell (2001). The errors resulting from the parallel beam presumption were revisited at the visualisation stage of the project, at which point it was decided they were small enough to leave the reconstruction process unchanged.

The effect of changing the exponent `alpha` of the raised-cosine filter on the reconstructed image for slice 431 of data set a are shown in Fig. 4, a scan taken directly opposite the X-ray source to avoid parallel beam presumption errors.

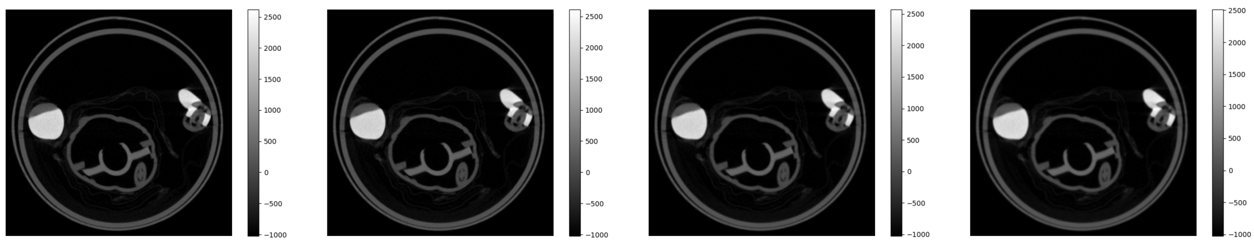

(a) Ram-Lak (b) `alpha` = 0.5 (c) `alpha` = 2.5 (d) `alpha` = 5

Figure 4: Reconstructions of slice 431 from data set a for various exponents of the raised-cosine filter.

Inspection of Fig. 4a, the reconstruction using the Ram-Lak filter, reveals very little in the means of streak artefacts. The Ram-Lak filter gives the optimal spatial resolution in the reconstructed image with minimal attenuation of noise [1]. Manifesting itself as streak artefacts in reconstructions, this observation indicates the CT data has little noise. Narrowing the band of the filter by increasing the exponent gave slight improvements in the signal-to-noise ratio (SNR), at the expense of significant diminishments in spatial resolution, as discussed in Section 4 of the Interim Report. This is particularly apparent in Fig. 4d, the reconstructed image using the largest exponent investigated of `alpha`=5, where the image is significantly blurred. Requiring a high resolution and a low degree of noise attenuation, a relatively small value of `alpha` = 0.5 was selected for the FBP process.

The form of the filter itself can be changed by applying a *window*, which involves multiplying the raised-cosine by another mathematical function. In doing so, the filter shape can be *tapered* to take a specific shape, such as a 'bell-shaped' curve to attenuate noise to a greater extent. Examples of windows include the *Hanning*, *Hamming* and *Shepp-Logan* functions, exact forms of which can be found in Oppenheim (1999). With little noise in the raw data, further investigations into reducing noise artefacts by changing the filter form were deemed unproductive, and the raised-cosine kept in the reconstruction function.

One significant drawback of CT is patient exposure to harmful, ionising X-ray radiation. As explained in Section 5 of the Interim Report, the dose is chosen to minimise the amount of radiation used whilst achieving an adequate SNR for cross-sectional imaging. Modifying the filter used in the reconstruction process is one means of increasing the SNR without delivering higher doses to the subject. This is viable up to a point, beyond which the image resolution becomes unacceptable and greater doses are required.

Beam hardening, the phenomenon by which occurs lower energy radiation is attenuated faster than higher energy radiation, was investigated in a similar manner for the CT data as with the phantoms for the CT simulator. Plots were made of the Hounsfield values along lines through the reconstructions taken at two different slice locations, the results of which are shown in Fig. 5. The first was the disk used for the Hounsfield conversion, a cross-section containing a large region of acrylic, a material with a low distribution of linear attenuation coefficients. The second was chosen as slice 220 of data set b. Fig. 5c, the reconstruction of this slice, shows two, much smaller regions of highly attenuating material, from which the action figure's thighs were made. A plot was made for a line partially passing through one of the thighs, as highlighted in Fig. 5c.

Interested in the underlying trend of Hounsfield values rather than the resolution of reconstructions, the exponent of the raised-cosine filter was set to a very large value of 10. In doing so, noise was attenuated to a high degree, reducing its impact on the data, consequently smoothing the plots. The smoothed plots, shown in Fig.s 5b and 5d, reveal fairly constant attenuation's through both the acrylic and thigh, indicating the X-ray beam energies are concentrated at the upper end of the energy spectrum. Having little impact on the accuracy of reconstruction, there seemed no need to correct for beam hardening.

Had there been more beam hardening, avoidance of 'cupping' artefacts would require a similar procedure to that used in the CT simulator: by first measuring the smoothed Hounsfield values HU_a through a range of different acrylic thicknesses t_a across the disk, a function $f(.)$ could be fit where $t_a = f(\mathrm{HU}_a)$. This function could then be used for the data to determine for each measured Hounsfield value HU_m what corresponding acrylic thickness $t_{a,m}$ would be needed to get this value. The *calibrated* Hounsfield value HU_c is then equal to a scaled version of the returned thickness $\mathrm{HU}_c = Ct_{a,m}$, where C is fixed such that HU_c=HU_m for an arbitrary low thickness of material.

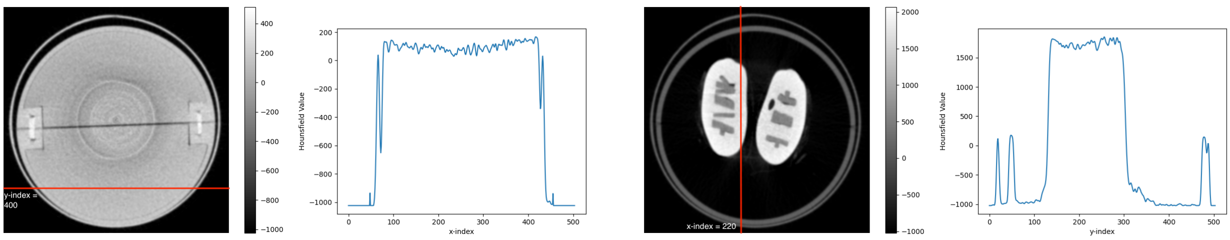

(a) (b) (c) (d)

Figure 5: Investigation into the extent of beam hardening within the CT data, reconstructed using a raised-cosine filter with `alpha` = 10. (a) Reconstruction of slice 25 from data set a, with an annotation of the line at a y-index of 400. (b) Variation in smoothed Hounsfield value with x-index at slice 25 and y-index of 400 for data set a. (a) Reconstruction of slice 500 from data set b, with an annotation of the line at an x-index of 220. (b) Variation in smoothed Hounsfield value with y-index at slice 500 and x-index of 220 for data set b.

4 Visualisation

CT reconstruction returns a huge amount of data, useful for treatment purposes only if utilised appropriately. Hence, specialist DICOM viewers were employed to effectively visualise the reconstructed 3D data sets. Choice of software was based off several factors, the first of which was that the software was free to download and run. With myself and Wong running MacOS systems, and Olieslagers Windows, we sought to use software that would be compatible for us all, such that we could easily compare results and not run into file format issues if sharing data within the team. These constraints narrowed down the pool of potential applications significantly, with the decision coming down to either **3DimViewer** or **3DSlicer**.

We investigated the functionality of each program by loading and viewing the provided low-resolution CT data. At only 1/4 the resolution of the scanner, visualising this data set was far less computationally expensive than the reconstructed raw data, allowing for key features of the software to be trialled quickly. **3DSlicer** was found to have a greater array of segmentation tools than **3DimViewer**, even extending to computed aided processes, as well as the ability to interpolate the data to a specified order. With more post-processing options and the capacity to import Python modules as extensions (should custom operations be required), **3DSlicer** gives increased control over the adjustable properties of the data. In addition, **3DSlicer** supports a wide range of medical imaging and 3D model file types, such as VTK and STL files, whereas **3DimViewer** can load only DICOM files. As such, **3DSlicer** allowed for greater flexibility in the subsequent stages of the project, where STL files used to model and print parts were loaded into and integrated with the scene containing the raw CT data. The superior functionality and file compatibility of **3DSlicer** made it the clear choice of visualisation software, subject to our constraints.

Errors introduced in making the parallel beam presumption in the reconstruction were clearly visible in the *Saggital* and *Coronal* 2D slices of volume images of the thighs. With 3 scans at either end of each z-fan overlapping with neighbouring z-fans and 41 z-axis scans at each source z location, jagged artefacts were present at consistent intervals of $41 - 3 - 3 = 35$ slices in the slice views, as shown in Fig. 6. Having identified these artefacts, we confirmed that they would not be an issue for our treatment plan; since they did not significantly affect the geometry of the figure, the fitting of the heart could still be established to a high accuracy.

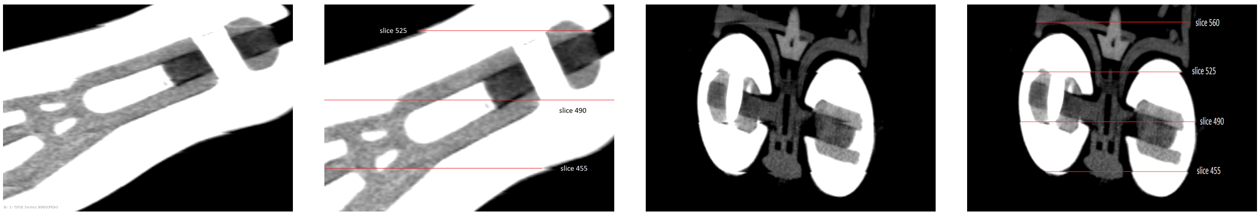

(a) (b) (c) (d)

Figure 6: 2D slice views of the thighs, images courtesy of Oliseslagers. (a) Saggital view. (b) Saggital view with artefacts highlighted and slices labelled. (c) Coronal view. (d) Coronal view with artefacts highlighted and slices labelled.

The task of 3D visualisation was handled mainly by Olieslagers and Wong. Between them, they applied various segmentation techniques to isolate the different parts of the action figure. *Thresholding* the data allowed for the figurine to be separated from the acrylic cylinder, the body taking significantly larger Hounsfield values than the cylinder in which it was mounted. The threshold level was very sensitive to noise: setting the value too low lead to the inclusion of many unwanted noise artefacts in the surface rendering, however increasing it even slightly resulted in regions on the figure in which matter was missed. It was decided to use conservatively low thresholds, such that complete surfaces of the subject were generated, with the issue of noise dealt with by *post-processing.*

Use of the *crop*, *paint* and *island* tools enabled delineation of each body part. Each part was assigned to a segment and so given its own colour, yielding an effective visual of the make-up of the subject. The surfaces were refined through the use of *filters*, which smoothed the data to remove extrusions and fill small holes [2]. In doing so, surface noise artefacts were eliminated and closed surfaces generated. Furthermore, the severity of the jagged artefacts resulting from the parallel beam presumption was suppressed. The form of the filter, either *Gaussian* or *median*, along with its corresponding parameters, were chosen based on which gave the best resulting surface on visual inspection. Processing the mesh in this way was the first step in preparing surfaces suitable for 3D printing.

The *logic* function was used to create a separate segment of the chest, as shown in Fig. 8a, which can be removed on the printed model to reveal the figure's internal structure. Compared to the original Action Man, this model lacks all clothing. Cloth, from which his clothing is comprised, is fairly porous, and as such is largely filled by air. Since it minimally attenuates X-ray beams, it is imaged poorly, being of similar Hounsfield value to the air within the scanner in the returned reconstruction. Whilst this is not a problem for medical imaging purposes, the focus being the patient's internal structure, it meant we were not able to obtain a complete reconstruction of the figure, accessories and all. His boots and belt-buckle, however, were attenuating enough to be thresholded and segmented, and as such were included in our model.

Rather than designing a heart ourselves, an actual CT scan of a patient's upper-chest was downloaded as a DICOM file from the OsiriX Image Library[1]. A limitation of reconstructed CT data is the inability to distinguish structures comprising of materials of similar linear attenuation coefficients. This issue became apparent why

[1] OsiriX DICOM Image Library, AGECANONIX, `https://www.osirix-viewer.com/resources/dicom-image-library/`

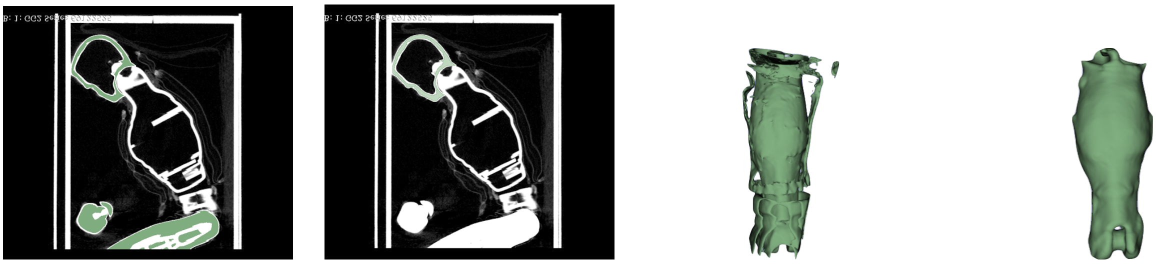

(a) (b) (c) (d)

Figure 7: Segmentation operations, images courtesy of Oliseslagers. (a) Thresholding to segment the head, thighs and hands from the acrylic cylinder and other body parts. (b) Island tool to isolate the head. (c) Original surface rendering of the lower leg, containing substantial noise artefacts and incomplete portions of trouser clothing. (d) Lower leg following filtering, in which the noise and clothing has been removed and a smooth surface generated.

trying to separate the heart from its surrounding frame. As such, a different set of segmentation methods were required. Wong successfully performed the *grow from seeds* operation in **3DSlicer**, a competitive region growing algorithm which automatically segments regions of data [10]. The heart was then mounted to the axle which runs horizontally within the action figure's chest, the results of which are shown in Fig. 8b.

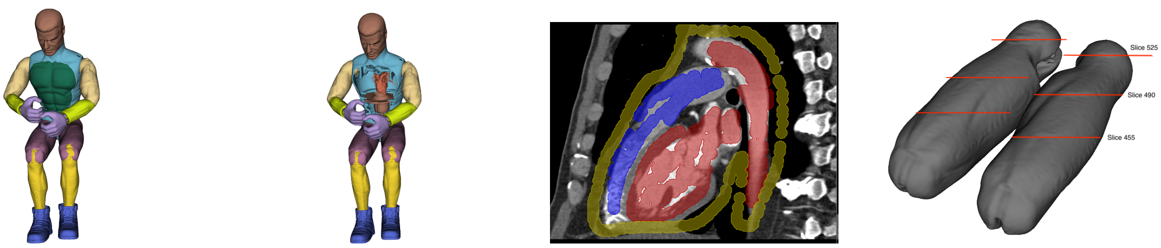

(a) (b) (c) (d)

Figure 8: Surface renderings of the segmented action figure. (a) Chest fitted to figure. (b) Chest removed to expose transplanted heart. (c) Slice view of heart, segmented using grow from seeds. (d) Subject's thighs, with discontinuity artefacts arising from the parallel beam assumption annotated at intervals of 35 slices. Images (a) and (b) courtesy of Olieslagers, and (c) Wong.

5 Modelling

With segmentation complete, the focus of attention turned to simulating the 3D print process to replicate the action figure. The investigation into modelling was carried out exclusively by myself. Progressing through this task, all major decisions and findings were conveyed to the other team members, thus ensuring everyone was on board with the direction in which the project was being taken.

Consisting of many parts with fine details, and desiring a high print resolution, the print simulation was based on the use of an **Ultimaker 2 Extended** printer. This is one of two types of printer available to students' in the Dyson Centre, the other being the lower definition, less versatile **RS/IdeaWerk Pro** [6].

The 3D model of the subject was first exported from **3DSlicer** as a *stereolithography* (STL) file, a neutral file format which simplifies the model into a representation that describes only the surface geometry, making it compatible with rapid prototyping devices [3]. The surface (or 'mesh') is defined in 3D Cartesian coordinates by a set of unstructured triangles unit normals and vertices consistently ordered by the right-hand rule.

To successfully print a model, the 3D surface must be closed and connected, giving a series of closed 2D contours that are partially filled during the print procedure. Furthermore, every edge must be shared by exactly two polygons and the surface should not self-intersect. A surface which satisfies the last two criteria is termed *manifold*. Since STL files do not enforce these properties, specialised surface processing software was employed to verify the suitability of each mesh before printing. As with the visualisation software, a free to use program with MacOS compatibility was required. Two such applications were compared: **MeshLab** and **Blender**. The former is a system devoted to the management and processing of meshes, containing a wide variety of tools aimed at *inspecting*, *healing* and *converting* large unstructured meshes. On the other hand, **Blender** is a more general 3D computer graphics system, equipped with features that enable animations, visual effects and motion graphics on top of 3D modelling. With so many options, presented on a rather complicated user interface, it was difficult to navigate through **Blender** to find sought after tools. However, turning to online documentation proved to be helpful. With a large community of users, and many tutorials available, learning the software was made somewhat easier. Becoming proficient in mesh manipulation using **Blender** allows for the production of far more aesthetic visuals than those possible in **MeshLab**, at the expense of time spent learning to use advanced features. With greater importance given to surface processing over visualising, it was decided that **MeshLab** would be sufficient for our needs.

Firstly, duplicate faces and vertices were removed, thus simplifying the surface. A 'watertight' check was performed to ensure each mesh was solid. This was achieved by the use of the `compute geometric measurements` function: if a volume was returned, the mesh was solid and complied to the check. Finally, a minimum wall thickness of 0.8 mm was enforced, guaranteeing a certain degree of wall durability without compromising on resolution.

The post-processed mesh was saved as an STL file and loaded into **Ultimaker Cura**, an open-source slicing application for 3D printers. Choice of this software was self-evident, being the accompanying program for **Ultimaker** printers, allowing for estimates of print time and material weight to be generated. To enable estimates of print cost, the price of a 750 g reel of 2.85 mm diameter 'Standard Black' polylactic acid (PLA) filament, that typically used in **Ultimaker 2 Extended** printers, was found from the ColorFabb website[2], ColorFabb cited as being the filament supplier for the Dyson Centre [6]. This information, alongside a standard configuration of printer settings as recommended by Thomas-McEwen (2017), was input into Cura, which returned an approximated cost of £0.36 m^{-1} filament printed. Other potential print materials, such as acrylonitrile butadiene styrene (ABS) and polyamide (PA), were researched, however issues with cost, 2.85 mm diameter availability and ventilation mean they are not permitted in the Dyson Centre [8], and so were excluded from the print investigation.

Prior to printing, the mesh must be *sliced*. This involves converting the surface described by the STL file into a set of specific instructions, usually in g-code format, for the 3D printer [3]. The object is first divided up into a set of stacked layers, which can be delivered sequentially by the printer, followed by the creation of printer commands to execute the process.

Wanting to replicate the entire body of the action figure, with the addition of a transplanted heart, a first, somewhat naive approach looked at printing the entire subject at once. The STL file was loaded into **Cura** and, using the default print settings, sliced in an upright position, as shown in Fig.s 9a and 9b. With much of the model suspended above the print bed, the issue of *support* quickly became apparent: 31% of the total print time was devoted to delivering plastic to prop overhanging and elevated regions. Without these structures, such regions would collapse during printing, having no previously solidified material below [3]. Since support is not part of the model, it must carefully be removed from the walls of the main body once the print process is complete. Particular care must be taken when separating support from thin features, as they tend to be brittle and so are easily broken by this action.

In an attempt to reduce the amount of support required, a different model orientation was investigated, in which the back of the action figure was laid horizontal and flat. It was only possible to achieve this by placing the figure diagonally across the print bed, as seen in Fig. 9c, the model otherwise exceeding the printer's allowable build volume. We were fortunate in that the entire model could be fit in any orientation with careful selection of its position in the print space. If the model exceeds the dimensions of the print bed, the user is restricted in the print configuration. Should there be no orientation which fits, the scale of the model must be reduced, or the model divided up into smaller sections to be printed separately. Changing the orientation had a significant impact on the print time and estimated print cost, with reductions of 5 hours and £2.58 respectively.

To eliminate the need for support for the model's suspended legs, it was decided to print each of the body parts individually and as close to the print bed as possible, making use of the segmentation achieved by Olieslagers and Wong in **3DSlicer**. The STL files for each part were loaded in turn and positioned on the print bed in a way which enabled all the elements to fit in the build volume. This layout can be seen in Fig. 10a. Upon slicing, it was noticed there were additional plastic structures surrounding the base of each component, as

[2]Standard Black 2.85 / 750 PLA, ColorFabb, `https://colorfabb.com/standard-black`

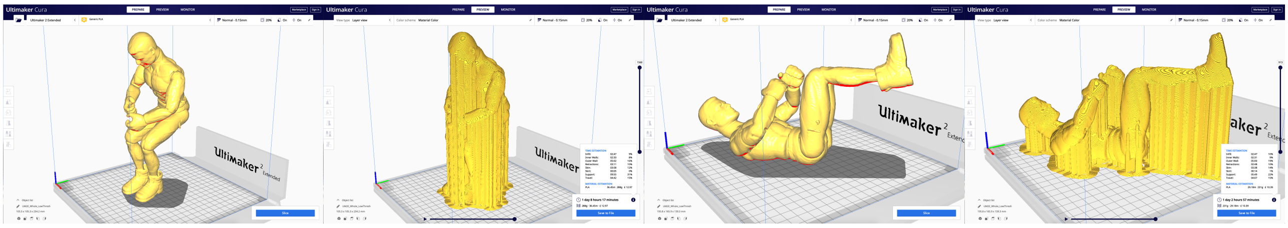

(a) (b) (c) (d)

Figure 9: Effect of model orientation on the printing process. (a) and (b): Vertical configuration prior and post slicing. (c) and (d): Horizontal configuration prior and post slicing.

shown in Fig. 10b. These structures are called *brim*, a single layer printed around the model to prevent warping during the print [7]. In addition to brim, each part was built onto *raft*, a thick grid of plastic printed between the model and the bed. Building the model on raft provides better adhesion to the build plate in instances when the bottom surface of the model is not completely flat, as was the case with all of the figurine's components. Both raft and brim fall under the category of *build plate adhesion* structures.

In printing a greater degree of the model directly onto the print bed, the segmented body part configuration called for twice as much build plate adhesion as the whole-body approach. Despite this, the overall print time was 3 hours 38 minutes faster and £2.30 cheaper, requiring 18.6% less PLA. This is due to the fact the reduction in support far outweighed the increase in build plate adhesion. Build plate adhesion is very thin, extending only a few layers from the print bed, compared to support which must reach the height of the feature it is propping. Hence, a decrease in support at the expense of an increase in adhesion is generally a worthwhile trade-off.

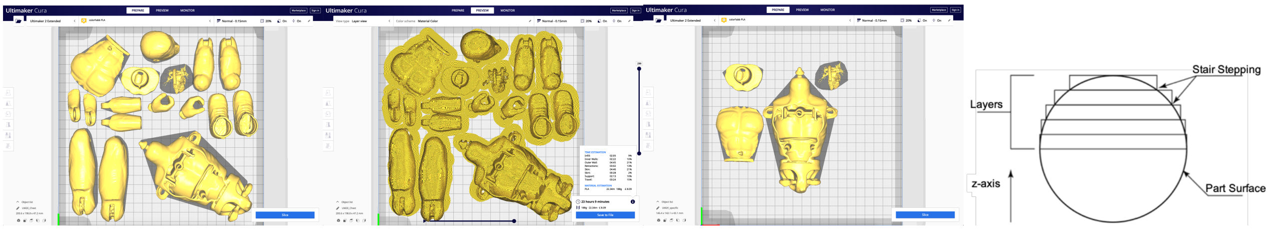

(a) (b) (c) (d)

Figure 10: Different model assembly options. (a) and (b): Body part assembly prior and post slicing. (c) Parts relevant to the heart transplant only. (d) Cross-section of a sliced sphere in the xz- plane, with 'stair-stepping' artefacts shown [3].

The resolution of the printed product is determined largely by the thickness to which the model is partitioned in the slicing process, known as the *layer height* [3]. Smaller layer heights yield improved surface quality and dimensional accuracy in the z-direction (height) of the model, as geometrical features are represented by thinner horizontal layers, reducing the degree of 'stair-stepping'. Stair stepping is analogous to aliasing of a line in 2D space which is neither horizontal nor vertical. Discretising the line by moves in the x- and y- axes creates a stepped representation of what should be a smooth, continuous line. Likewise in 3D printing, a geometrical feature which is not parallel with the horizontal or vertical planes will be interpreted by a series of discrete shifts between layers. The formation of these artefacts is shown for a sphere in Fig. 10d.

The other commonly changed print parameters are *infill density* and *infill pattern*. Infill density defines the extent to which 2D contours are filled with plastic in the print. Using a higher infill density increases the amount of plastic within between the walls of the print, resulting in a stronger object. For **Ultimaker 2 Extended** printers, an infill density of 20% is sufficient for models with a "purely visual purpose" [7]. Infill patterns can be sub-divided into two categories: 2D and 3D. 2D patterns are faster to print, but fall short on strength compared to 3D patterns.

Since our treatment plan involved the transplant and fitting of a heart within the action figure, it was decided to focus our investigations on the four body parts directly involved in the procedure. Changes to the weight of PLA used, print cost and print time for the four-part assembly shown in Fig. 10c were explored for each of the print parameters in turn, the results of which are summarised in Table 1. The first row in the table is the configuration to which each change was compared, being the default settings in **Cura**. Two different infill patterns were investigated. The *grid* pattern is a 2D infill pattern, typically used for everyday prints, whereas *octet* is a much stronger 3D infill, with the additional benefit of the object being equally strong in all directions [7].

Table 1: Effect of print parameters on print properties for the four-part assembly shown in Fig. 10c. Entries in bold are settings which have been changed from the default configuration in row 1.

Layer Height (mm)	Infill Density (%)	Infill Pattern	Weight (g)	Cost (£)	Print Time (hh:mm)
0.15	20	Grid	78	3.35	10:20
0.1	20	Grid	77	3.32	15:12
0.15	30	Grid	80	3.44	10:35
0.15	20	Octet	78	3.34	10:20
0.1	30	Octet	79	3.41	15:28

There were only slight variations in print weight and cost as the quality of print was increased, the maximum values for which were both obtained when the infill density was raised to 30% and the layer height and infill pattern kept constant at their baselines. The percentage increases in weight and cost were 2.6% and 2.7% respectively- very small differences. The print time was only significantly impacted when the layer height was reduced from 0.15 to 0.10 mm. This change resulted in almost a 50% increase in print time. These results, alongside those from the investigation into model orientation, suggest that all three print properties are governed by the size of model and extent to which support is required, with print time also being affected by the layer height. Equipped with this knowledge, the print parameters of all body parts were refined.

The body parts not specific to the transplant procedure were chosen to be printed using the default **Cura** print parameters, as outlined in the first row of Table 1, in order to cut down on print time.

It was decided to use a layer height of 0.10 mm, infill density of 30 % and octet infill pattern for the replica's torso (the three leftmost components shown in Fig. 10c). As the original components of Action Man relevant to the heart transplant, these parts needed to be of adequate strength, to ensure they would withstand the demands of the fitting of the heart onto the final figure.

The heart itself was the most intricate structure to be printed. An extra fine layer height of 0.06mm was selected for this print, the high resolution chosen in an attempt to preserve as many of it's details and features. The improvement in smoothness of the heart's surface by reducing the layer height from 0.10 to 0.06 mm is evident by comparing the sliced models, displayed in Fig.s 11a and 11b respectively. Due to the fact it is such a small component, there was only a 40 minute increase in print time.

With the print settings described, the total print time for the entire model was 1 day 2 hours 40 minutes. Using 189 g of PLA, the cost of production was £8.15.

An issue not resolved by decreasing the layer height is the need to remove support from the model once the print process is complete. Many of the blood vessels which branch off the heart are relatively thin structures. Hence, removal of support risks damaging the model. There is no way of knowing whether the heart would survive the support removal procedure without actually printing the part. It therefore seemed sensible to have contingency plans for the case the heart was found to be too delicate upon printing.

The first workaround involved scaling up the model. In doing so, the size of each parts was increased uniformly in all directions. Printed with more plastic, model strength is improved, reducing the likelihood of damages in the removal of support and build plate adhesion. A scaling of 175% was chosen, being the largest size at which the figure's torso could fit within the build volume when laid horizontally. Another advantage of printing at a higher scale is an enhancement in resolution: the same part is printed to 175% the height it was previously, and as a result, is comprised of 175% the layers. The degree of stair-stepping is therefore reduced. However, this comes at the expense of increases in both print material and print time. For the heart alone, the print time rose from 1 hour 39 minutes to 5 hours 53 minutes, an increase of 257%, with the cost increasing by a factor of 4.75. To keep print costs and time down, only the four body parts relevant to the heart transplant would be printed at a higher scale, enabling the fitting of the heart to be effectively modelled. A separate model consisting only of the original Action Man parts would be printed at a 1:1 scale, allowing for physical investigations into the accuracy and effectiveness of the full-body CT reconstruction and surface segmentation.

In the event that the 175% scale heart was still too fragile, an alternative, simpler heart design was found, this time as an STL file from the embodi3D file library[3]. Lacking the smaller blood vessels, this heart is far more likely to be successfully printed and processed. The STL file was shared with Olieslagers and Wong, who confirmed a means by which this heart could be fitted to the figurine. Slicing this model, the results of which are shown in Fig. 11d, yields a much less complicated surface, which gave confidence in its chances of successful post-print processing.

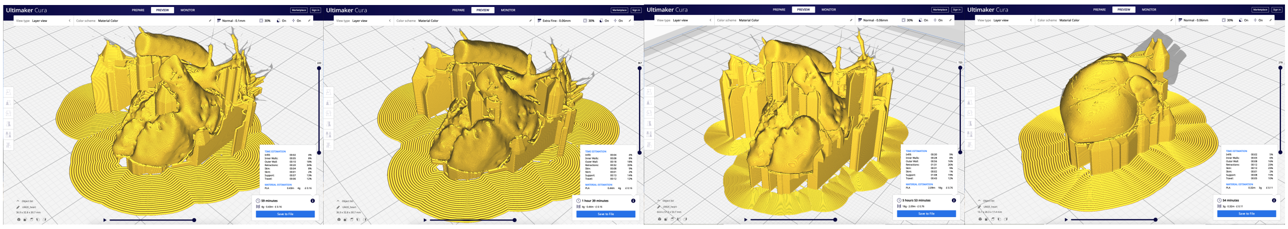

(a) (b) (c) (d)

Figure 11: Different heart print options. (a) Slicing at a 0.10 mm layer height. (b) Slicing at a finer 0.06 mm layer height. (c) Slicing at 175% scale and a 0.06 mm layer height. (d) Alternative, simpler heart model; sliced at a 0.06mm layer height.

6 Group Reflection

Working with Olieslagers and Wong was a hugely enjoyable experience. From our first meeting, we were agreed on wanting to complete each task to the best of our abilities. United in this goal, we each set about developing the CT simulator for ourselves, striving to understand the purpose of every function and its operation, sharing insights along the way and providing assistance where required. The environment we created was very stimulating, and conflicts were always resolved quickly and maturely. There was never a stigma around asking questions or querying why someone had done something in a certain way. I believe this is the reason we each learnt so much: our knowledge of the content was at a level where we could succinctly explain it to either teammate.

The group really came into its own in the second half of the project. Wong and I focused on the investigations around reconstruction, Olieslagers and Wong produced the segmented surface, and finally, I simulated the 3D printing process. Although we divided ourselves up, we were always aware of what was going on within each sub-team. Brainstorming as a group sprouted methods and ideas that we would not have thought of individually.

The only real group issue we encountered was that of the time difference: with Olieslagers and Wong being eight hours ahead, I quite often found I had a huge amount of catching up to do upon waking, as they worked during the day in their native timezone, which corresponded to times when I would be asleep.

It is down to the work of the project leader, Dr Graham Treece, whose dedication and devotion to providing a stimulating, engaging project ultimately led to this assignment being such a success. Thanks must also go to Dr Alexandre Kabla, who's insights in our daily meetings helped tremendously in directing us with where to focus our attention. Together, they ensured we had the best possible support during such a difficult and unfamiliar situation, for which I am incredibly grateful.

7 Conclusion

The process of CT reconstruction can be tailored to the object being scanned and geometry of scanner. The cylinder in which the action figure was mounted was used to make the conversion from attenuation to Hounsfield units, eliminating the need for a water scan. With a small beam angle, errors made in the presumption that the cone-beam was parallel were slight and sparse, only occurring at the end of each z fan. From visual inspections, it was concluded there was little noise in the reconstructions, which led to the selection of a raise-cosine filter with a small exponent for the FBP process. Furthermore, it was shown the data had a low-degree of beam hardening, which as a result was not corrected for.

[3]embodi3D, 3D printable human heart, `https://www.embodi3d.com/files/file/35-3d-printable-human-heart/`

Use of freely available software enabled both 2D slice views and 3D visualisations of the reconstructions. Utilising the features of these packages, the figurine was segmented into its constituent body parts and a heart fitted. Issues regarding separation of regions of similar attenuation were overcome by means of more sophisticated segmentation methods.

The surfaces generated were post-processed in two stages: firstly, they were healed to remove holes, smooth noise and reduce artefacts, before being checked for watertightness and wall thickness. A detailed investigation into print parameters was made, from which a configuration was selected to print all the body parts of the action figure at specified layer heights and infills. Whilst 3D printing of the model can be simulated, giving estimates for print time, cost and material weight, it does not encompass the full production process; support removal and model strength tests can only be achieved by physically printing. Upon printing, it may be found that changes to the scale or structure of the model are required.

References

[1] Thorsten Buzug. *Computed Tomography- From Photon Statistics to Modern Cone-Beam CT*, pages 247–252. Springer, Berlin, 2010. ISBN 9783642072574.

[2] Andriy Fedorov, Reinhard Beichel, Jayashree Kalpathy-Cramer, Julien Finet, Jean Christophe Fillion-Robin, Sonia Pujol, Christian Bauer, Dominique Jennings, Fiona Fennessy, Milan Sonka, John Buatti, Stephen Aylward, James V. Miller, Steve Pieper, and Ron Kikinis. 3D Slicer as an image computing platform for the Quantitative Imaging Network. *Magnetic Resonance Imaging*, 30(9):1323–1341, Nov 2012. ISSN 0730725X. doi: 10.1016/j.mri.2012.05.001.

[3] Todd Grimm. *User's Guide to Rapid Prototyping.* Society of Manufacturing Engineeers, Dearborn, Mich, 2004. ISBN 978-0872636972.

[4] SCANCO Medical. *XtremeCT: Preclinical microCT: Systems & Solutions: SCANCO Medical: micro CT scanners, image analysis software, microtomography scan services*, May 2020 (accessed 26 May, 2020). http://www.scanco.ch/en/systems-solutions/preclinical/xtremect-preclinical.html.

[5] Alan V. Oppenheim. *Discrete-Time Signal Processing*, pages 465–472. Prentice Hall, 2nd edition, Jan 1999. ISBN 0137549202.

[6] Richard L. Roebuck. *3D Printing- Dyson Centre for Engineering Design*, Aug 2019 (accessed 2 Jun, 2020). https://www.dysoncentre.eng.cam.ac.uk/3d-printing/3d-printing-default-page.

[7] Ultimaker Support. *Print Settings*, Mar 2020 (accessed 2 Jun, 2020). https://support.ultimaker.com/hc/en-us/sections/360003548619-Print-settings.

[8] Diana Thomas-McEwen. *User manual for Ultimaker 2 Extended 3D printer (V1).* Dyson Centre for Engineering Design, Department of Engineering, University of Cambridge, Sept 2017.

[9] Henrik Turbell. *Cone-Beam Reconstruction Using Filtered Backprojectionn.* PhD thesis, Linköping University, 2001.

[10] Vladimir Vezhnevets and Vadim Konouchine. GrowCut- Interactive multi-label N-D image segmentation by cellular automata. *GraphiCon 2005 - International Conference on Computer Graphics and Vision, Proceedings*, 2005.